Kuan Zheng
School of Aeronautics and Astronautics,
Shanghai Jiao Tong University,
Shanghai 200240, China
e-mail: zhengkuan@sjtu.edu.cn

Wei Tian[1]
School of Aeronautics and Astronautics,
Shanghai Jiao Tong University,
Shanghai 200240, China
e-mail: tianwei@sjtu.edu.cn

Peng Zhang
School of Mechanical Engineering,
Shanghai Jiao Tong University,
Shanghai 200240, China
e-mail: zhangpeng828@sjtu.edu.cn

Yu Rao
School of Mechanical Engineering,
Shanghai Jiao Tong University,
Shanghai 200240, China
e-mail: yurao@sjtu.edu.cn

Hui Hu
Department of Aerospace Engineering,
Iowa State University,
Ames, IA 50011
e-mail: huhui@iastate.edu

Experimental Study of Turbulent Flow and Heat Transfer Behaviors Over a Micro-Rib-Dimple-Structured Surface

An experimental study was conducted to characterize the evolution of turbulent boundary layer flow over a micro-rib-dimple-structured surface. In addition to measuring the surface pressure distribution and detailed flow field inside the dimple cavity, the heat transfer performance over the rib-dimpled surface was investigated using transient liquid crystal thermography. The flow field measurements were correlated with the heat transfer measurements to elucidate the underlying physical mechanism of the improvement in thermal efficiency due to the micro-rib structure. It was found that, compared to the dimpled surface, the micro-rib structure induces a stronger downwash flow and acts as a turbulator to enhance the turbulent mixing of the downstream flow, which significantly restricts the flow separation and the recirculating flow inside the dimple cavity. The dominant flows inside the dimple cavity are the downwash and successive upwash flows, which significantly enhance the turbulent mixing and, consequently, improve the heat transfer performance over the rib-dimpled surface. The measurements of the pressure loss and heat transfer performance indicated that the rib-dimpled surface has an overall thermal efficiency approximately 12–16% higher than that of the dimpled surface owing to the micro-rib structure.
[DOI: 10.1115/1.4050946]

Keywords: rib-dimpled surface, flow field, heat transfer, particle image velocimetry (PIV), transient liquid crystal (TLC) thermography

1 Introduction

The thermal efficiency of gas turbine engines is highly related to their turbine inlet temperature. Based on this notion, the inlet temperature has been increased continuously to meet the demand for increased turbine efficiency. As a result, to make the hot gas path components withstand extreme thermal loads, innovative internal cooling methods with high cooling efficiency are urgently required. A dimpled surface, which can significantly enhance the heat transfer with relatively low-pressure loss, is an effective cooling strategy in forced convective heat transfer and provides a convenient alternative for the internal cooling of hot gas path components.

A number of studies have been conducted recently to investigate the heat transfer performance of dimpled surfaces through both experiments [1–6] and numerical simulations [7–10]. Kim et al. [1] compared three different cooling strategies (i.e., strip-strips, jet array impingement, and dimples) in a wide Reynolds number region (i.e., $26{,}000 < \mathrm{Re} < 360{,}000$). They indicated that the dimpled channel tends to stand out as the most effective cooling scheme in terms of the overall thermal performance. Afanasyev et al. [2] and Terekhov et al. [3] reported the achievement of a considerable heat transfer enhancement (30–40%) for dimpled surfaces with no appreciable effect on the pressure loss relative to a smooth surface. Their results also indicated that the aerodynamic resistance caused by the dimple is much smaller compared to the heat transfer efficiency [2,3]. Ligrani et al. [11] and Mahmood et al. [12] argued that the enhancement of the heat transfer efficiency over the dimpled surface is due to the shedding of vortices from the dimple edge and the flow upwash in the rear region of the dimple. Recently, Zhou et al. [13] experimentally quantified the flow characteristics inside the dimples and described the formation and periodic shedding of unsteady Kelvin–Helmholtz vortices in the shear layer over the dimple cavity.

In addition, the geometry and configuration of the dimple have been shown to have an important effect on the heat transfer performance of the dimpled surface. Burgess and Ligrani [4] experimentally measured the channel heat transfer performance with various dimple depths. Their results revealed the enhancement in the heat transfer efficiency with the increase in the dimple depth, which is caused by the increasing strength of shedding vortices with higher turbulence production and transportation. Moon et al. [14] and Mahmood and Ligrani [15] investigated the effects of channel height on heat transfer behavior. Moon et al. [14] indicated that the overall enhancement in heat transfer was almost independent of the channel height at Reynolds numbers from 12,000 to 60,000. However, at Reynolds numbers from 600 to 11,000, the data of Mahmood and Ligrani [15] indicated that stronger vortex pairs are shed by the dimple with a lower channel height, resulting in higher local heat transfer enhancements. Coy and Danczyk [16] found that the heat transfer enhancement increased as the depth-to-diameter ratio increased when the fraction of the surface covered by dimples was larger than 0.5. In addition to the normal spherical dimple, the non-spherical dimple configurations were also considered by many researchers. Chyu et al. [17] examined the heat transfer enhancement with teardrop- and spherical-shaped dimples and found that both configurations can induce higher heat transfer enhancement than a spherical dimple. Jordan and Wright [18] measured the heat transfer distributions of surfaces with V-shaped dimples and concluded that the V-shaped dimple is a promising alternative to hemispherical dimples, especially under high Reynolds numbers. Rao et al. [19] systemically

[1]Corresponding author.

Contributed by the Heat Transfer Division of ASME for publication in the Journal of Turbomachinery. Manuscript received October 12, 2020; final manuscript received April 7, 2021; published online May 19, 2021. Assoc. Editor: Stephen Lynch.

investigated the effects of the dimple shape on the heat transfer and pressure loss of a dimpled surface with four different dimple shapes: spherical, teardrop, elliptical, and inclined elliptical. The results showed that the surfaces with teardrop dimples had the highest heat transfer efficiency, which was approximately 18% higher than that of the spherical dimples.

Although the dimpled surface can significantly enhance the convective heat transfer performance, detailed experimental and numerical calculations showed that at the front portion of the dimple, the enhanced heat transfer efficiency is relatively low compared to that at the rear region of the dimple; this is mainly due to the flow separation with the low-speed recirculating flow at the front portion of the dimple cavity. It was found that the heat transfer coefficient of the front portion of a spherical dimple is only 25% or even lower than that of the rear region [11,19]. Rao et al. [19] indicated that teardrop dimples can partly improve the heat transfer performance in the region near the front rim. However, the teardrop shape is complicated and difficult to manufacture, especially machining on turbine blades with complex geometry.

Rib turbulators can effectively enhance heat transfer performance. Han and coauthors [20–23] systematically studied the effects of the rib turbulator geometry, rotational speed, and entrance condition on the heat transfer performance inside internal cooling passages. Choi et al. [24,25] combined the angled rib and dimple as a novel rib-dimple compound cooling strategy. Their results indicated that the rib-dimple cooling had the greatest thermal-hydraulic performance (THP) compared with the single-handed rib or dimple cooling. A similar conclusion was also reported for the combination of V-shaped ribs and spherical dimples in a two-pass channel [26]. Singh et al. [27] investigated the effects of the rib shape, including 45 deg angled V, W, and M shapes, on the heat transfer performance of rib-dimple surfaces. However, they considered a ratio of rib height to channel hydraulic diameter between 0.078 and 0.125. Such large rib turbulators would cause very high pressure loss, which is much higher than the pressure loss due to the dimples.

In order to decrease the pressure loss caused by the rib turbulators, micro V-shaped ribs (i.e., the ratio of rib height to channel hydraulic diameter is only 0.023) are introduced to combine with the spherical dimples in the present study. The flow induced by the micro-ribs was expected to further interact with the low-speed recirculating flow inside the spherical dimples and enhance the turbulent kinetic energy, thereby increasing the heat transfer efficiency over the dimpled surface, especially at the front of the dimple cavity. Compared with the complicated dimple geometries such as teardrop dimple, the manufacture of the spherical dimple is more realistic for the internal cooling channel of gas turbine engines. In addition, the convex structures over the surface of the internal cooling channel, such as pin fin, rib turbulator, have been widely applied in modern gas turbine engines. Therefore, the micro V-shaped rib proposed in this study can be easily processed in engineering applications.

In the present study, the experiments were conducted in a low-speed wind tunnel at the Shanghai Jiao Tong University. The Reynolds number (based on the channel hydraulic diameter and the freestream velocity) was set in the range of 18,700–60,000. The flow characteristics over the micro-rib-dimple-structured surface were measured using surface pressure taps and high-resolution digital particle image velocimetry (PIV), while the heat transfer performances were examined using transient liquid crystal (TLC) thermography. The flow and heat transfer characteristics of a pure dimpled surface were also measured for comparison.

2 Experimental Setup and Validation

2.1 Test Model. The experimental study was performed in a low-speed, open-circuit wind tunnel located at Shanghai Jiao Tong University. A rectangular channel was designed to simulate the flow inside the internal cooling channel of the turbine blades. The tunnel has an optically transparent test section with a cross section of 20 mm × 120 mm and a corresponding hydraulic diameter D_h of 42.9 mm. The turbulence intensity level of the airflow in the test section of the wind tunnel was approximately 1.0%. The inflow velocity at the inlet of the test section ranged from 8.0 m/s to 26.0 m/s. As indicated by Han and Chen [23], the typical Reynolds number based on the channel hydraulic diameter ranges from 10,000 to 80,000 for the turbine blades of an aircraft engine. In the present study, the Reynolds number based on the channel hydraulic diameter and the inflow velocity was calculated to be between 18,700 and 60,000, which is in the range of the typical Reynolds number of channel flow to investigate the internal cooling of aircraft engine turbine blades [19,28]. In addition, a screen heater located in front of the test section was connected to a high-power direct current (DC) power supply. The airflow was quickly heated to approximately 50 °C through the mesh heater and flowed into the test section.

Figure 1 shows the schematic of the micro-rib-dimple-structured test plate as well as a dimpled test plate. As shown in the figure, the two test plates are designed with the same dimensions (i.e., 245 mm in length and 130 mm in width). Spherical dimples with a diameter of 20 mm and depth of 4 mm were distributed uniformly on both test plates with a staggered pattern. The distances between adjacent dimples in the spanwise and streamwise directions are 25 mm and 21.6 mm, respectively. For the micro-rib-dimple-structured test plate, V-shaped ribs with a thickness of 1 mm are placed in front of the dimples, and the pitch sizes of the ribs are the same as those of the dimples in both the streamwise and spanwise directions.

As indicated by Chyu et al. [29] and Chang et al. [30], the turbulent flow over a surface with dimple arrays can be divided into a developing region and a fully developed region. The turbulent flow and heat transfer behavior would reach a stable state after a certain number of dimple rows. The present study focuses on the fully developed region. Therefore, the rib dimple at the middle of row 7 was selected to study the turbulent flow and heat transfer behaviors of a typical micro-rib-dimple structure, as shown in Fig. 1.

There were 15 pressure taps with a diameter of 0.5 mm arranged over the dimpled surface to measure the pressure distributions inside the dimple cavity, as shown in Fig. 1. The pressure taps were linked to a unit of digital sensor arrays (DSA3217, Scanivalve Corp) through Tygon tubing with a 1.5 mm diameter and a 0.3 m length for the pressure data acquisition. The accuracy of the pressure acquisition sensor was ±0.05% of the ±10 inch H_2O full-scale range. During the experiments, the measurement data for each pressure tap were collected with a data acquisition rate of 300 Hz for 300 s.

2.2 Experimental Setup for Particle Image Velocimetry Measurements. PIV measurements were taken to acquire the detailed flow field inside the dimple cavity, as shown in Fig. 2. The incoming airflow was seeded with ~1-μm oil droplets produced by a fog seeding machine. The light pulse was generated by a frequency-doubled dual cavity 380 mJ Nd:YAG pulse laser at a wavelength of 532 nm. The thickness of the laser sheet in the measurement region was approximately 0.5 mm. A high-resolution 14-bit (2048 pixels × 2048 pixels) charge-coupled device (CCD) camera (PCO2000, Cooke Corp) was used to collect the PIV images. The timing of the CCD camera and the doubled-pulsed laser was controlled by a digital delay generator (BNC-575, Berkeley Nucleonics) with fixed time sequences, which were set to control the individual procedure steps.

In order to capture the flow field inside the dimple cavity, an angle of 21 deg between the view axis of the CCD camera and the horizontal plane normal to the illuminating laser sheet (i.e., the x–y plane) was set during the PIV measurements, as shown in Fig. 2. A tilt-axis mount was installed between the camera body and the lens to satisfy the Scheimpflug condition and focus the tracer particles in the laser sheet in the image plane. As the image plane of the camera was not parallel to the laser sheet, the images

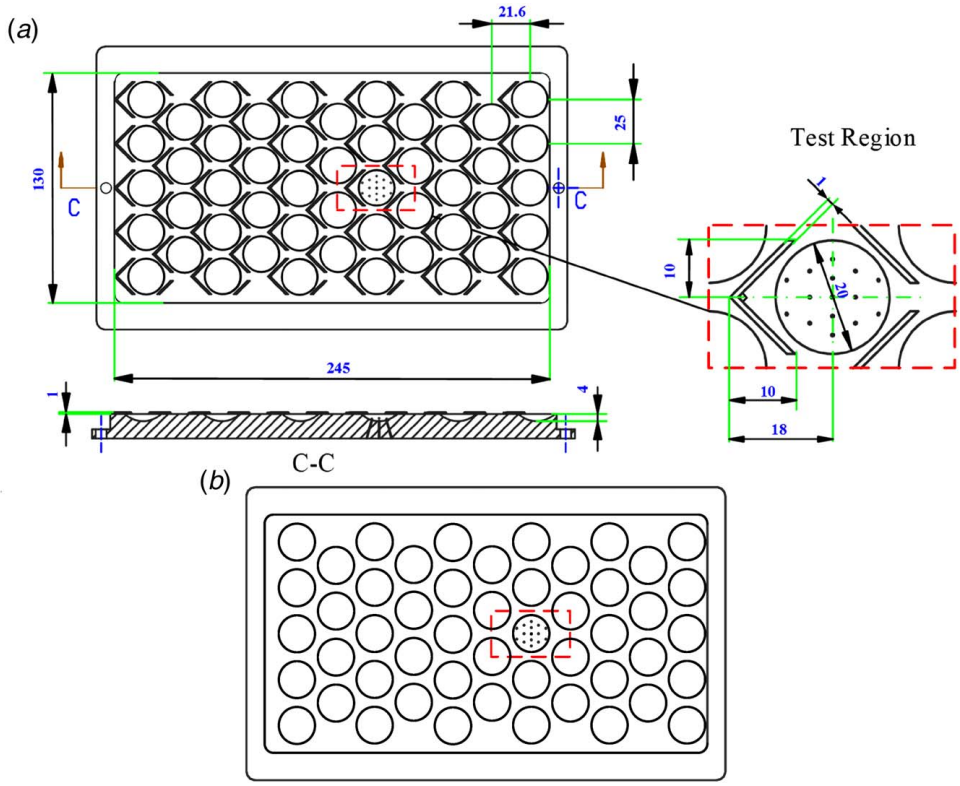

Fig. 1 Schematic of (*a*) rib-dimple-structured test plate and (*b*) dimpled test plate (unit in mm)

were deformed and the magnification factors between the image plane and the object plane were variable. Therefore, the in situ calibration procedure reported by Soloff et al. [31] was used to get the quantitative mapping functions to calculate the velocity distribution inside the dimple cavity. The test plates were covered with a layer of Rhodamine 6G paint to reduce the negative effect of laser reflection. The fluorescence induced by the laser from the Rhodamine 6G coated surfaces was filtered using a 532-nm bandpass filter mounted in front of the lens of the CCD camera.

After PIV image acquisition, instantaneous velocity vectors were obtained by frame-to-frame cross-correlation of particle images using an interrogation window of 32×32 pixels. An effective overlap of 50% of the interrogation window was employed in PIV image processing. A sequence of 300 frames of instantaneous results were averaged to obtain the distributions of the ensemble-averaged flow quantities, such as the averaged velocity, Reynolds shear stress, and in-plane turbulent kinetic energy (TKE). The measurement uncertainty level for the instantaneous velocity vectors was estimated to be within 2.0%, while the uncertainties for the measurements of the ensemble-averaged flow quantities were estimated to be within 5.0%.

2.3 Experimental Setup for Transient Liquid Crystal Measurements. The heat transfer coefficient was calculated based on data measured by TLC thermography with a one-dimensional (1D) semi-infinite conduction solid model. The tested surface was manufactured from a low thermal conductivity

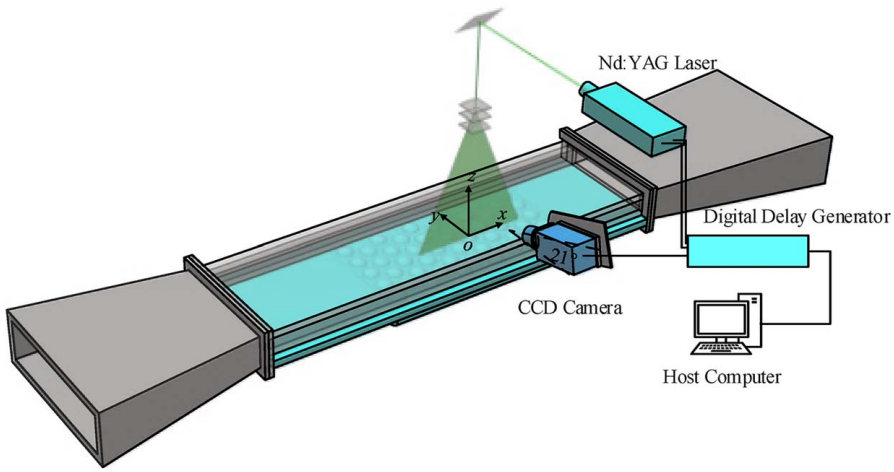

Fig. 2 Schematic of the experimental setup for PIV measurements (*x*–*z* plane crossing the center of the tested surface)

material (Plexiglas). The low conductivity allows heat to flow into the tested surface purely one-dimensionally (z-direction), so that the lateral conduction (in the x–y plane) can be neglected. The transient heat transfer model of the solid is expressed as follows:

$$k\frac{\partial^2 T}{\partial z^2} = \rho c \frac{\partial T}{\partial t} \tag{1}$$

The initial condition and boundary conditions are expressed as follows:

$$t = 0,\ T(z, 0) = T_i$$

$$z = 0,\ -k\frac{\partial T}{\partial z} = h(T_r - T_w)$$

$$z \to \infty,\ T(z, t) = T_i$$

where T_i, T_w, and T_r are the initial temperature of the Plexiglass, the temperature of the wall surface exposed to the air, and the temperature of the airflow, respectively; h, k, ρ, and c are the heat transfer coefficient, thermal conductivity, density, and specific heat capacity of the Plexiglass, respectively. The analytical solution for the heat conduction with convective heat transfer boundary condition on the mainstream side and the constant temperature boundary condition on the other side of the solid is expressed as

$$\frac{T_w - T_i}{T_r - T_i} = 1 - \exp\left(\frac{h^2 t}{k\rho c}\right) erfc\left(h\sqrt{k\rho c t}\right) \tag{2}$$

However, Eq. (2) is valid only for a constant mainstream temperature T_r, which is not satisfied during transient experiments. In actual transient experiments, the mainstream temperature is not time independent. In order to consider the transient nature of the mainstream temperature, Duhamel's superposition principle is applied to the model. The resulting equation can be written as follows [26]:

$$T_w = T_i + \sum_{j=1}^{N} (T_{r,j} - T_{r,j-1}) \times \left[1 - \exp\left(\frac{h^2(t - t_j)}{k\rho c}\right) erfc\left(h\sqrt{k\rho c(t - t_j)}\right)\right] \tag{3}$$

where $T_{r,j}$ is the mainstream bulk temperature at the specific time t_j, and T_w is the wall temperature at time t. The mainstream bulk temperature T_r was recorded by two calibrated thermocouples (Type-K, Omega) placed at the entrance of the test section, and the wall temperature T_w were obtained by TLC measurements. Both the thermocouple and TLC measurements were operated under the same frequency of 25 Hz. The Nusselt number (Nu) is defined as

$$\mathrm{Nu} = \frac{hD_h}{k} \tag{4}$$

The experimental setup of the TLC is shown in Fig. 3. To improve the TLC color visibility for the image acquisition, the test plate was first covered with black paint. The TLC used in the experiments had a nominal red start temperature of 35.1 °C with a bandwidth of 1 °C. A CCD video camera with a rate of 25 fps was used to monitor the change in the TLC color. From the relationship between the temperature and color, the time history of the temperature distribution over the tested surface was obtained. The heat transfer coefficient h was then be calculated using Eq. (3) from the temperature information. The TLC was calibrated in situ on the present test section before the experiments with the same fluorescent lighting and viewing conditions. The TLC calibration setup consisted of a copper block, thermocouple, and electric heater. The maximum error of the measured Nusselt number was less than ±8.5%. During the TLC measurements, in order to avoid the optical distortion induced by the curved surface of the dimple cavity, the in situ calibration procedure reported by Soloff et al. [31] was also adopted to obtain the mapping functions between the curved dimple surface and the image plane to determine the Nusselt number distribution inside the dimple cavity.

A comparative study was performed to validate the reliability of the results measured by the TLC technique. Figure 4 shows the comparison of the measured Nusselt number along the longitudinal centerline of dimple with the results of Mahmood and Ligrani [15] obtained by using infrared thermometry technique. It should be noted that the Reynolds number defined by Mahmood and Ligrani [15] is based on the height of the test section, while the Reynolds number shown in Fig. 4 is calculated based on the channel hydraulic diameter. Therefore, the Reynolds number in Fig. 4 (i.e., Re = 19,400) is a recalculated value, which corresponds to the Reynolds number of 10,300 in the study of Mahmood and Ligrani [15]. As shown in Fig. 4, the main heat transfer features over the dimpled surface agree well with the results given by Mahmood and Ligrani [15]. Some discrepancies are believed to be caused by the differences in dimple geometry and test condition.

3 Results and Discussion

3.1 Surface Pressure Distributions Inside the Dimple Cavity. The distributions of the pressure coefficient $C_P (C_P = (P - P_\infty)/(1/2)\rho U_0^2)$, where P_∞ and U_0 are the static pressure and average velocity of the inflow at the entrance of the test plate were measured by 15 pressure taps arranged in the dimple cavity, as shown in Fig. 1. Figure 5 shows the pressure distributions inside the dimple cavity with a rib-dimpled surface under different Reynolds numbers. The pressure distributions over the dimpled test plate are also plotted for comparison.

For the dimpled test plate, it can be observed that the measured pressure distributions are quite similar at different Reynolds numbers. Similar trends were also reported by Zhou et al. [13]. A region with low pressure exists near the front rim of the dimple,

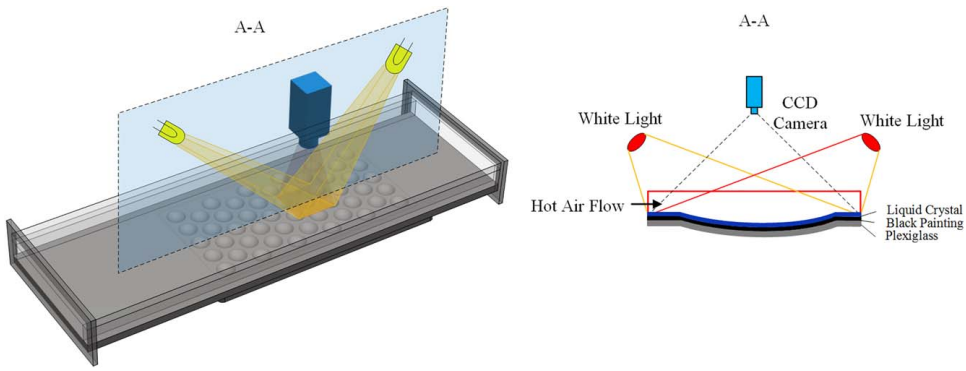

Fig. 3 Schematic of TLC measurements

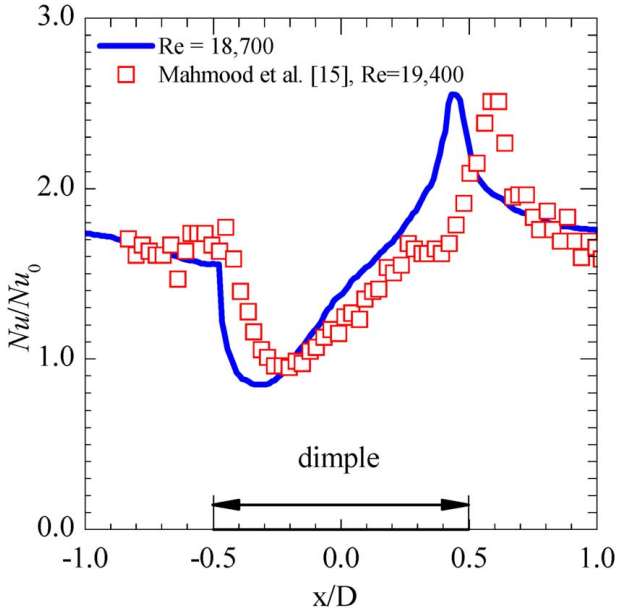

Fig. 4 Comparison of the measured Nusselt number along the longitudinal centerline of the dimple

while the pressure is high in the region near the back rim of the dimple. This pressure distribution pattern is attributed to the flow characteristics over the dimple. The incoming flow separated as it passes the front rim of the dimple, resulting in the formation of a recirculation zone with relatively low pressure and a rather flat surface pressure distribution at the front portion of the dimple. While the pressure near the front rim of the dimple is relatively low, the incoming flow with high pressure moves downward and impinges upon the back rim of the dimple, leading to a high-pressure region near the back rim of the dimple.

For the rib-dimpled test plate, the pressure distribution pattern inside the dimple cavity shows distinct differences compared with that of the dimpled test plate. It can be seen that the pressure increases continuously along the flow direction at the front portion of the dimple cavity, while that of the dimpled test plate remains constant. This reveals that the recirculation flow inside the dimple cavity, which induces a low and constant pressure distribution, is weakened significantly by the micro-rib located in front of the dimple cavity. In addition, it can be seen that the highest value of the pressure occurs at $x/D = 0.2$ for the rib-dimpled surface, while it occurs at $x/D = 0.4$ for the dimpled surface without micro-rib structure, which indicated that the existence of the micro-rib led to the forward movement of the flow impingement point.

3.2 Flow Characteristics Over the Rib-Dimpled Surface. The flow characteristics over the dimpled and rib-dimpled surfaces at Re = 50,500 are shown in Figs. 6 and 7, respectively. For the dimpled surface, it can be seen from Figs. 6(*a*) and 6(*b*) that the incoming boundary layer flow separates as it passes the front rim of the dimple. The front part of the dimple is fully filled with the recirculating flow, which is consistent with the flat pressure distribution shown in Fig. 5(*e*). In addition, owing to the existence of the low pressure caused by the recirculating flow at the front part of the dimple cavity, the high-speed incoming boundary layer flow deflects slightly downward and impinges onto the back rim of the dimple. Then, a strong upwash flow appears downstream of the impingement point. This impingement of the high-speed incoming flow creates a high-pressure region near the back rim of the dimple cavity, which is also revealed from the pressure distribution shown in Fig. 5(*e*). These flow structures inside the dimple cavity shown in Fig. 6 were found to agree well with the studies of Ligrani et al. [32] and Han et al. [33]. Figure 6(*c*) shows the instantaneous velocity field over the dimpled surface. It can be seen that the flow structure inside the dimple is fairly complicated and is filled with numerous unsteady vortex structures with different sizes and orientations. These vortices mainly originate from the shear layer between the high-speed incoming boundary layer flow and the low-speed recirculating flow inside the dimple cavity.

As mentioned previously, for the dimpled surface, the unsteady vortex structures were found to be generated along the interface between the high-speed incoming flow and the low-speed recirculating flow inside the dimple cavity. The turbulent mixing in the boundary layer over the dimple cavity is enhanced by these unsteady vortex structures; thus, the high TKE region appears in the shear layer region between the high-speed main flow and the low-speed recirculating flow, as shown in Fig. 6(*d*). In addition, the upwash flow near the back rim of the dimple would significantly enhance the turbulent mixing between the low momentum flow near the wall and the high momentum incoming flow. Therefore, as can be seen from Fig. 6(*d*), a region with high in-plane TKE appears near the back rim of the dimple.

For the rib-dimpled surface, it can be seen clearly from Figs. 6 and 7 that the flow characteristic is significantly changed owing to the existence of the micro-rib located upstream of the dimple cavity. The micro-rib structure induces a strong downwash flow, which restricts the flow separation when the flow passes the front rim of the dimple. It can be seen that the recirculation zone inside the dimple cavity is much smaller than that of the dimpled surface, which agrees with the shrinkage of the flat pressure distribution region at the front portion of the dimple cavity, as displayed in Fig. 5(*f*). In addition, the comparison between Figs. 6(*b*) and 7(*b*) shows that the impingement position of the high-speed incoming flow moves forward owing to the reduction in the flow separation region inside the dimple cavity for the rib-dimpled surface. As a result, the flow upwash region behind the impingement point expands significantly compared to that in the dimpled surface case. As mentioned in Sec. 3.1, the impingement of the high-speed flow would lead to a high-pressure region. Thus, it can be seen in Figs. 5(*e*) and 5(*f*) that compared to the dimpled surface case, the location corresponding to the highest value of surface pressure moves forward for the rib-dimpled surface.

Figure 7(*c*) shows the instantaneous velocity field over the rib-dimpled surface. It can be seen that owing to the shrinkage of the recirculation zone inside the dimple cavity, the shear layer between the high-speed incoming flow and the low-speed recirculating flow is not obvious. Consequently, the unsteady vortex structures originating from the shear layer become much smaller and weaker, so they cannot be clearly observed in Fig. 7(*c*). Therefore, in contrast to the dimpled surface case, the turbulent mixing of the flow inside the dimple cavity is not contributed by the unsteady vortices originating from the shear layer for the rib-dimpled surface case.

However, as shown in Fig. 7(*d*), even though the unsteady vortices originating from the shear layer are highly restricted by the upstream micro-rib structure, the region with high in-plane TKE is much larger in the rib-dimpled surface than in the dimpled surface. This wide range with high in-plane TKE is mainly caused by two reasons. First, the distinct downwash and upwash flows inside the dimple cavity significantly enhance the fluctuation of the flow velocity, thereby increasing the turbulent level of the flow inside the dimple cavity. Second, the micro-rib structures act as turbulators to increase the turbulence mixing of the downstream flow. Therefore, it can be seen from Fig. 7(*d*) that compared to the dimpled surface, the high in-plane TKE appears in a much wider range above the plate surface for the rib-dimpled surface case. In addition, the enhanced turbulent mixing of the flow after the rib results in a fuller boundary layer velocity profile, thereby delaying the downstream flow separation inside the dimple cavity. Ligrani et al. [11] reported that the flow in the region with a high in-plane TKE experiences enhanced turbulent mixing, which is closely related to the improved local heat transfer performance. Therefore, the data shown in Figs. 6(*d*) and 7(*d*) reveal that the rib-dimpled surface should have a much better heat transfer performance than

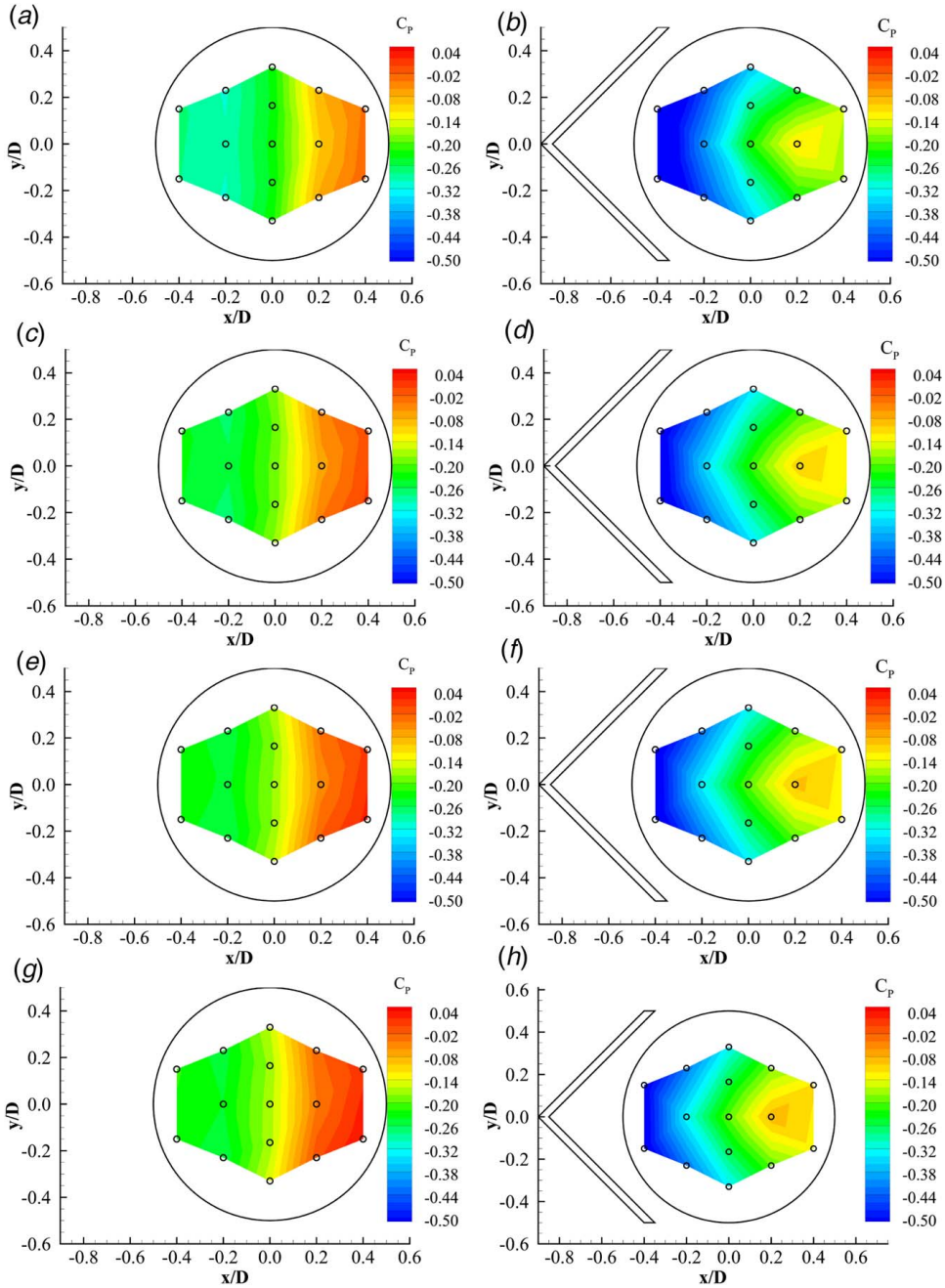

Fig. 5 Measured surface pressure coefficient distributions inside the dimple cavity for the dimpled and the rib-dimpled surfaces under different Reynolds numbers: (*a*) Re = 18,700, dimpled surface; (*b*) Re = 18,700, rib-dimpled surface; (c) Re = 36,700, dimpled surface; (*d*) Re = 36,700, rib-dimpled surface; (e) Re = 50,500, dimpled surface; (*f*) Re = 50,500, rib-dimpled surface; (*g*) Re = 60,000, dimpled surface; and (*h*) Re = 60,000, rib-dimpled surface

the dimpled surface. More importantly, the low heat transfer efficiency at the front portion of the dimple can be significantly improved by implementing a micro-rib structure upstream.

For the dimpled surface, Zhou et al. [13] indicated that the Reynolds number mainly influences the recirculating flow inside the dimple cavity. With the increase in the Reynolds number, the recirculating flow inside the dimple cavity becomes stronger and the center of the recirculation zone moves forward to the front rim of the dimple. Figure 8 shows the flow characteristics over the rib-dimpled surface measured by PIV for the test cases with Re = 36,700 and 60,000. It can be seen from Figs. 8(*a*) and 8(*b*) that owing to the significant shrinking of the recirculation zone, the general flow pattern inside the dimple cavity is quite similar under different Reynolds numbers. In addition, it can be observed from Figs. 8(*e*) and 8(*f*) that the value of the in-plane TKE is higher at Re = 60,000 than at lower Reynolds numbers (i.e., Re = 36,700); this indicates that the Reynolds number mainly influences the turbulent mixing of the flow over the rib-dimpled surface.

Figure 9(*a*) shows a schematic of the flow structures over the rib-dimpled surface determined based on the PIV and pressure distribution measurements. The schematic of the flow features over the dimple surface reported by Zhou et al. [13] is plotted in Fig. 9(*b*) for comparison. For the dimpled surface (Fig. 9(*b*)), the incoming boundary layer flow cannot resist the adverse pressure gradient caused by the dimple cavity; therefore, the boundary layer flow

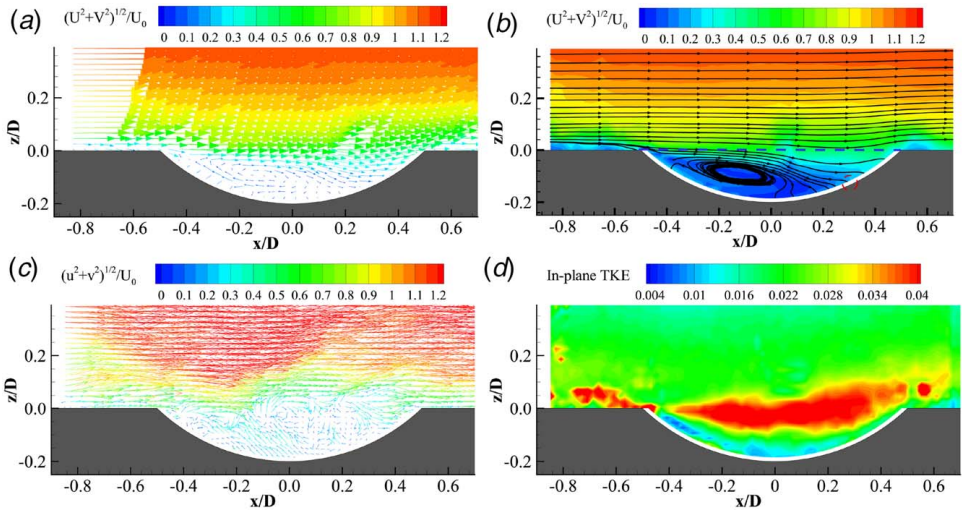

Fig. 6 Flow characteristics in the longitudinal central plane of the dimple for the dimpled surface at Re = 50,500: (*a*) Ensemble-averaged velocity vector; (*b*) streamline of the mean flow field; (*c*) instantaneous velocity field; and (*d*) in-plane TKE distribution

would separate at the front rim of the dimple and form a low-speed recirculating flow region inside the dimple cavity. The unsteady vortex structures originating from the shear layer would highly increase the turbulent mixing between the high-speed incoming flow and the low-speed recirculating flow inside the dimple cavity. In addition, owing to the existence of low pressure at the front part of the dimple cavity, the high-speed main flow has a downward deflection and impinges onto the back rim of the dimple. After the impingement, the flow is divided into two streams with one stream recirculating inside the dimple and the other moving out of the dimple to induce a strong upwash flow.

For the rib-dimpled surface, the flow structure inside the dimple cavity is significantly different from that of the dimpled surface. The upstream micro-rib would generate a strong downwash flow and enhance the turbulent mixing of the boundary layer flow, thereby restricting the downstream flow separation inside the dimple cavity. Therefore, the recirculation zone is much smaller than that of the dimpled surface. The impingement position of the main high-speed flow moves forward to the front rim of the dimple cavity. The flow features inside the dimple cavity of the rib-dimpled surface are dominated by a distinct downwash and successive upwash flow, which would significantly increase the turbulence level of the flow over the rib-dimpled surface.

3.3 Local Heat Transfer Characteristics for the Rib-Dimpled Surface. The heat transfer characteristics of the dimpled and rib-dimpled surfaces were measured by the TLC thermography system, as mentioned in Sec. 2.3. The results were normalized by the Nusselt number of a fully developed turbulent flow in a smooth channel, which can be calculated according to the Dittus–Belter correlation [34] as follows:

$$\mathrm{Nu}_0 = 0.023\mathrm{Re}^{0.8}\mathrm{Pr}^{0.4} \tag{5}$$

where Re is the Reynolds number based on the hydraulic diameter of the channel, and Pr is the Prandtl number of air. The ratio $\mathrm{Nu}/\mathrm{Nu}_0$ indicates the heat transfer enhancement by the dimpled or rib-dimpled surfaces compared to a smooth channel.

The local heat transfer characteristics for the rib-dimpled surface at different Reynolds numbers are shown in Fig. 10. The results for the dimpled surface are also plotted for comparison. For the dimpled surface, the heat transfer performance at the front portion

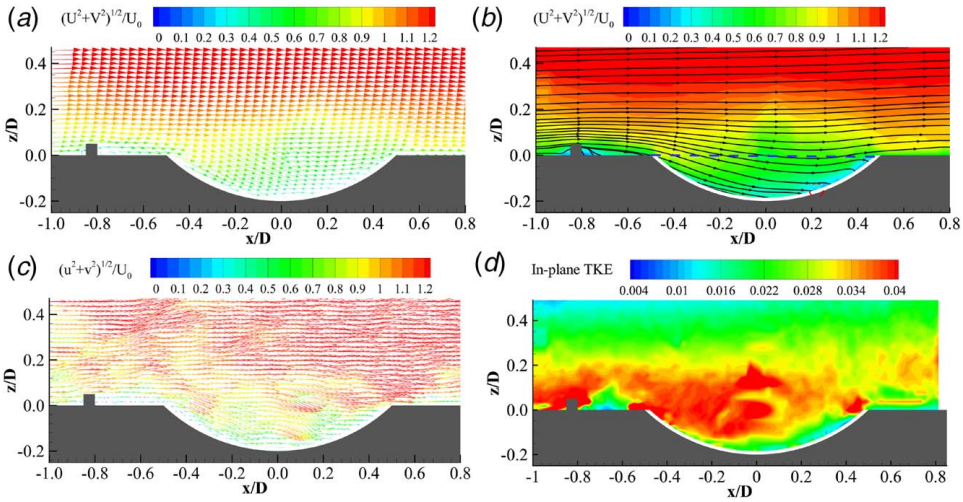

Fig. 7 Flow characteristics in the longitudinal central plane of the dimple for the rib-dimpled surface at Re = 50,500: (*a*) ensemble-averaged velocity vector; (*b*) streamline of the mean flow field; (*c*) instantaneous velocity field; and (*d*) in-plane TKE distribution

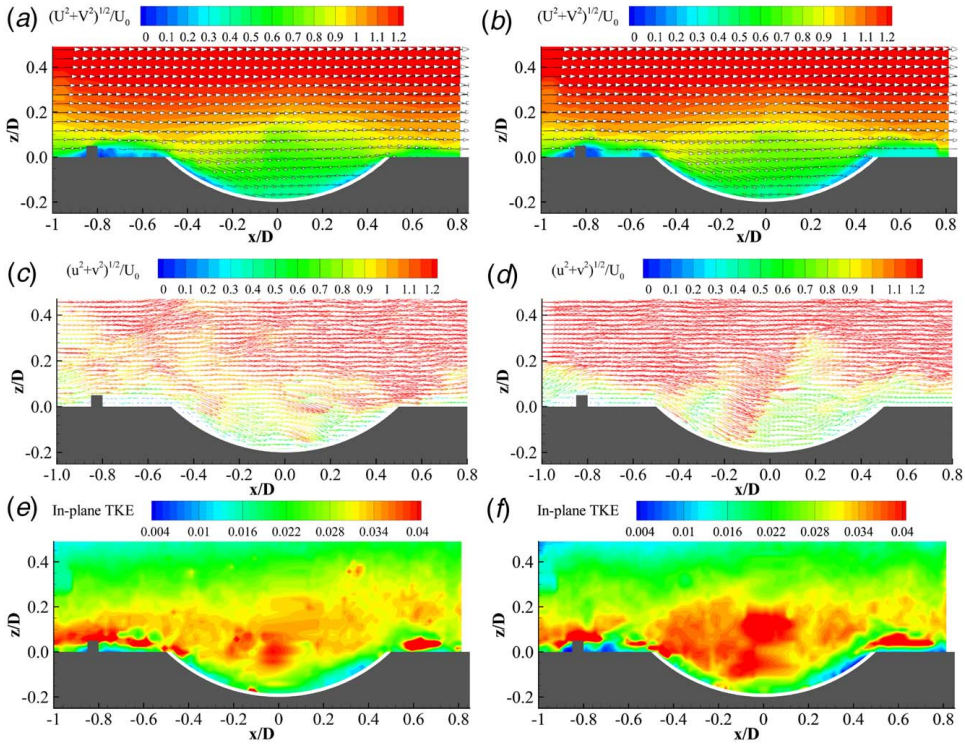

Fig. 8 Comparison of the flow characteristics in the longitudinal central plane of the dimple for the rib-dimpled surfaces at Re = 36,700 and 60,000: (*a*) Re = 36,700, ensemble-averaged velocity field; (*b*) Re = 60,000, ensemble-averaged velocity field; (*c*) Re = 36,700, instantaneous velocity field; (*d*) Re = 60,000, instantaneous velocity field; (e) Re = 36,700, in-plane TKE distribution; and (*f*) Re = 60,000, in-plane TKE distribution

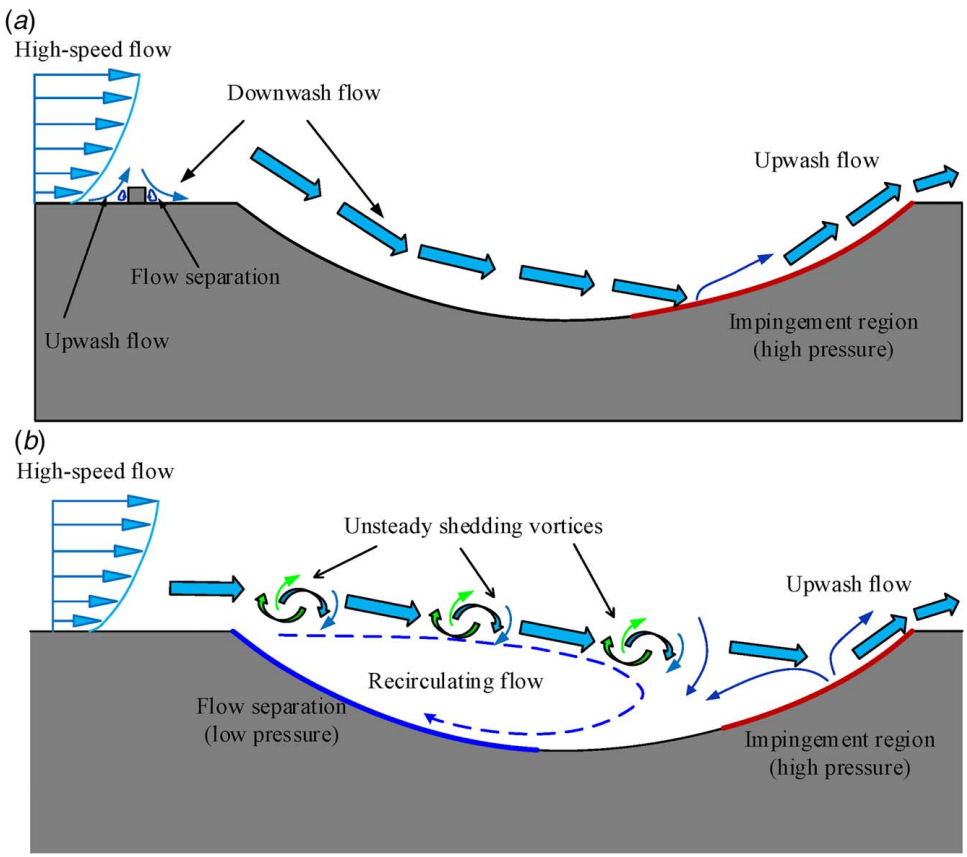

Fig. 9 Schematics of the flow structure inside the dimple cavity of (*a*) rib-dimpled surface and (*b*) dimpled surface [13]

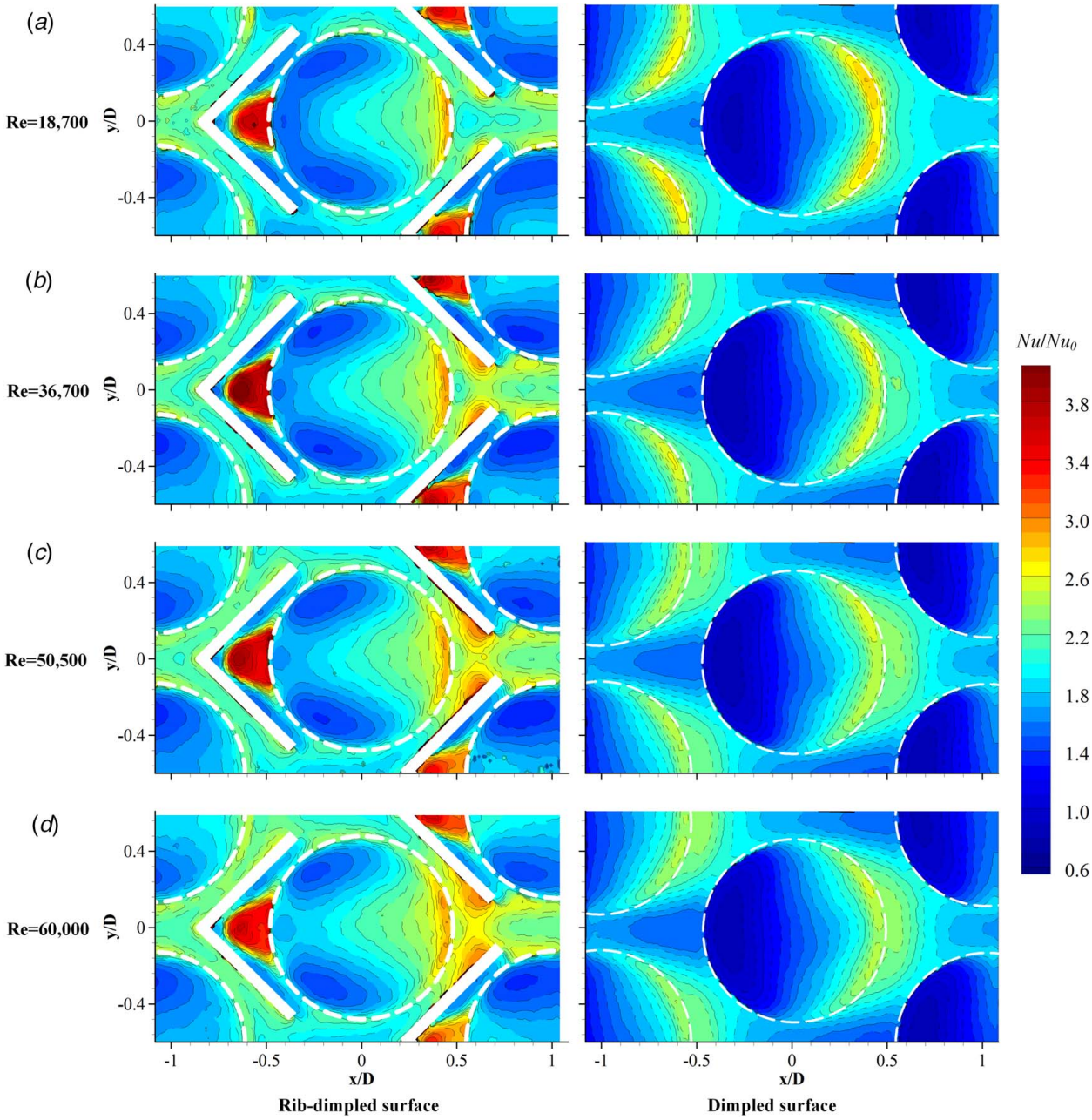

Fig. 10 Contours of local Nusselt number for the rib-dimpled and dimpled surfaces under different Reynolds numbers

of the dimpled cavity is rather poor owing to the flow separation and the recirculating flow inside the dimple cavity, as shown in Fig. 9(*a*). It can be seen that in the region $x/D = -0.5 - 0.25$, the value of Nu/Nu_0 is below one, which indicates that the heat transfer performance is weakened by the existence of the dimple cavity compared to the smooth surface. Downstream of the recirculation zone, the impingement of the high-speed flow, and the successive upwash flow over the back portion of the dimple would enhance the local heat transfer performance. Therefore, it can be seen that the value of Nu/Nu_0 increases continuously as the downstream distance increases over the back portion of the dimple. Similar trends of the Nusselt number distribution over a dimpled surface were also reported by Mahmood and Ligrani [15].

From Fig. 10, it is apparent that compared to the dimpled surface, the heat transfer performances are significantly improved owing to the existence of the upstream micro-rib structure. There is a region with high Nu/Nu_0 just between the rib and the front rim of the dimple mainly due to the strong downwash flow induced by the micro-rib, as shown in Fig. 9(*a*). Owing to the delay in the flow separation and the significant shrinkage of the recirculation zone, the region with the value $Nu/Nu_0 < 1$ inside the dimple cavity disappears for the rib-dimpled surface. The value of Nu/Nu_0 increases along the longitudinal centerline of the dimple with the increase in the downstream distance and reaches a maximum near the back rim of the dimple cavity.

The Nu/Nu_0 profiles along the longitudinal centerline of the dimple are shown in Fig. 11. It can be clearly seen that owing to the effect of the upstream micro-rib, the heat transfer performance along the longitudinal centerline is much higher than that of the dimpled surface. The heat transfer performance near the front rim of the dimple cavity is always relatively high for the rib-dimpled surface. There are two peak values of Nu/Nu_0 for the rib-dimpled surface: one between the rib and the front rim of the dimple and the other near the back rim of the dimple. The former is related to the strong downwash flow induced by the micro-rib, and the latter mainly corresponds to the strong upwash stream after the

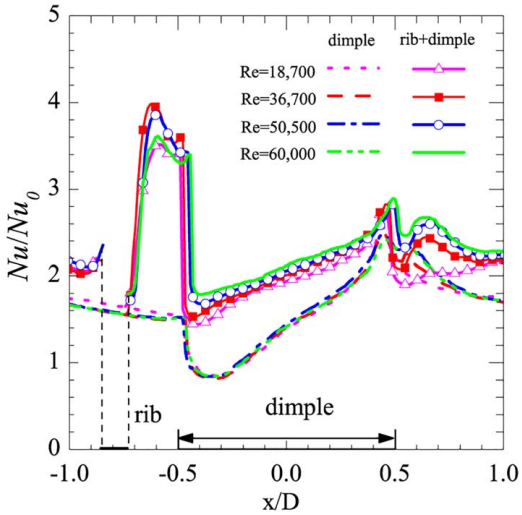

Fig. 11 Profiles of Nu/Nu_0 along the longitudinal centerline for the dimpled and rib-dimpled surfaces

high-speed main flow impinging onto the surface of the dimple cavity.

As shown in Fig. 10, the Reynolds number has no evident effect on the value of Nu/Nu_0 over the dimpled and the rib-dimpled surfaces within the Reynolds number range selected in the present study. The change of Nu/Nu_0 along the longitudinal centerline of the dimple is plotted in Fig. 11. It can be seen that the Nu/Nu_0 show slight change with the variation of Reynolds number. Similar trends were also reported by Burgess and Ligrani [4] and Choi et al. [25] in the study of the dimpled surface. Han and Zhang [21] investigated the heat transfer performance over a pure rib surface and found that the effect of the downwash flow induced by the rib on the heat transfer enhancement becomes weaker with increasing Reynolds number. As shown in Fig. 11, for the rib-dimpled surface, the magnitude of Nu/Nu_0 in the region between the rib and the front rim of the dimple decreases as the Reynolds number increases. In addition, for the region inside the dimple cavity, the value of Nu/Nu_0 on the surface shown in Fig. 11 increases with increasing Reynolds number. This phenomenon is highly related to the fact that the increasing Reynolds number enhances the turbulent mixing of the flow inside the dimple cavity, as revealed in Figs. 8(*e*) and 8(*f*).

3.4 Comparison of the Pressure Loss Between the Dimpled and Rib-dimpled Surfaces. In the present study, the pressure loss Δp across the test plate was calculated by measuring the static pressures upstream and downstream of the test plate. The normalized pressure loss can be defined by the friction factor f

$$f = \frac{2\Delta p D_h}{\rho U_0^2 L} \tag{6}$$

where L is the length of the test plate.

According to the Blasius formula, the friction coefficient of a fully developed turbulent flow in a smooth channel can be calculated as follows:

$$f_0 = 0.316\mathrm{Re}^{-0.25} \tag{7}$$

The friction factors, which were normalized by the friction coefficient of a fully developed turbulent flow in a smooth channel (i.e., f/f_0), are listed in Table 1. As expected, the pressure loss due to the existence of a micro-rib structure is greater for the rib-dimpled surface than that for the dimpled surface. In the studied Reynolds number range, the pressure losses for the rib-dimpled surface are approximately 45–52% higher than those of the dimpled surface

Table 1 Friction factors of rib-dimpled and dimpled surfaces

	f/f_0	
Re	Rib-dimpled surface	Dimpled surface
18,700	2.73	1.88
36,700	2.86	1.93
50,500	3.09	2.05
60,000	3.21	2.11

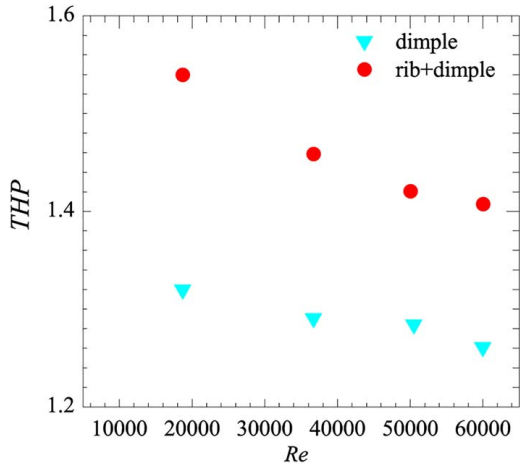

Fig. 12 THP of dimpled and rib-dimpled channel as a function of the Reynolds number

and approximately 2.7–3.2 times greater than those of the smooth channel. It should be noted that this increase in pressure loss is much smaller than that caused by conventional rib turbulators placed inside the internal cooling channel [20–25]. Compared with the results of Choi et al. [25], in order to obtain a similar heat transfer enhancement (i.e., Nu/Nu_0) corresponding to the rib-dimpled surface, the pressure losses caused by the conventional rib turbulators are approximately $6.0 \sim 7.5$ times greater than those of the smooth channel (i.e., $f/f_0 = 6.0 \sim 7.5$).

The heat transfer enhancement per unit pressure loss of the test plates was evaluated considering the THP, which represents the heat transfer enhancement of the test plate under the same pumping power [35]

$$\mathrm{THP} = \frac{(\overline{\mathrm{Nu}}/\mathrm{Nu}_0)}{(f/f_0)^{1/3}} \tag{8}$$

where $\overline{\mathrm{Nu}}$ is the global averaged Nusselt number, i.e., the area-averaged value of the Nusselt number Nu of the test region shown in Fig. 10.

Figure 12 shows the THP of both the dimpled and rib-dimpled surfaces under different Reynolds numbers. It can be seen that the thermal-hydraulic efficiency decreases gradually with the increase in the Reynolds number, which is consistent with the experimental results of Singh and coauthors [26,27]. More importantly, it can be seen that the THP of the rib-dimpled surface is approximately 12–16% higher than that of the dimpled surface. This enhancement in the THP indicates that by implementing a micro-rib structure in front of the dimple cavity, the thermal efficiency inside the internal cooling channel of a turbine blade can be improved.

4 Conclusion

An experimental investigation was conducted to study the flow and heat transfer characteristics over a rib-dimpled surface in the

Reynolds number range of 18,700–60,000. In addition to the detailed pressure distribution inside the dimple cavity measured by using pressure transducers, a high-resolution PIV system was employed to further elucidate the evolution of the flow structure over the test plates. In addition, the heat transfer performance of the test plates was measured using a TLC thermography system. The flow field measurements were correlated with the heat transfer measurements to elucidate the underlying physical mechanism of the improvement in the thermal efficiency by the micro-rib structure.

The measurement results clearly reveal that the micro-rib structure induces a strong downwash flow and acts as a turbulator to enhance the turbulent mixing of the downstream flow. These effects of the micro-rib highly restrict the flow separation when the flow passes the front rim of the dimple, and the recirculation zone inside the dimple cavity becomes much smaller than that of the dimpled surface. In addition, for the rib-dimpled surface, the impingement position of the incoming high-speed flow moves forward owing to the reduction in the flow separation region inside the dimple cavity. The flow features inside the dimple cavity are dominated by a distinct downwash and successive upwash flow, which significantly increase the turbulent kinetic energy of the flow over the rib-dimpled surface.

Owing to the change in the turbulent characteristics over the test plates, the heat transfer performances are significantly improved by the existence of the upstream micro-rib structure. The region with relatively low heat transfer performance due to the recirculating flow inside the dimple cavity disappears for the rib-dimpled surface. In addition, the pressure loss analysis shows that the micro-rib structure increases the pressure loss by approximately 45–52% within the tested Reynolds number range. However, the overall thermal efficiency of the rib-dimpled surface was enhanced by approximately 12–16% compared to the dimpled surface. Therefore, the combination of the micro-rib and downstream dimple structure can be used to further improve the thermal efficiency inside the internal cooling channel of turbine blades.

It should be noted that the inlet turbulence intensity in the present study is approximately 1%. In fact, the flow turbulence inside cooling channels of the turbine blades changes over a wide range. Ligrani et al. [36] experimentally studied the effects of inlet turbulence level on the Nusselt numbers and flow structure on and above a dimpled surface. Their results indicated that the Nusselt number ratios (i.e., Nu/Nu_0) decrease slightly with the increase of inlet turbulence intensity. This slight decrease of Nu/Nu_0 is mainly caused by the increased turbulent diffusion of vorticity and diminished magnitudes of vortex secondary flow shed by the dimples. As revealed in Sec. 3.2, the flow structure inside the dimple is significantly changed due to the existence of the micro-rib. Therefore, more extensive researches are still needed to quantify the influences of inlet turbulence intensity on the flow structures and heat transfer behaviors over a micro-rib-dimple-structured surface.

Acknowledgment

The support from the National Natural Science Foundation of China (Grant Nos. 51676119, 11972230, and 11872039) is gratefully acknowledged.

Conflict of Interest

There are no conflicts of interest.

Data Availability Statement

The data sets generated and supporting the findings of this article are obtainable from the corresponding author upon reasonable request. The authors attest that all data for this study are included in the paper. Data provided by a third party are listed in Acknowledgment.

Nomenclature

c = specify heat capacity of the plexiglass, J/(kg · K)
f = friction factor
h = heat transfer coefficient, W/(m^{2}K)
k = thermal conductivity of the Plexiglass, W/(mK)
t = time
D = dimple diameter
L = length of the test plate
P = static pressure, Pa
T = temperature, K
f_0 = friction coefficient based on the Blasius formula
C_p = pressure coefficient
D_h = channel hydraulic diameter
P_∞ = static pressure at the inlet of the test section
U_0 = average velocity of the inflow at the inlet of the test section
Nu = local Nusselt number
Nu_0 = local Nusselt number based on the Dittus–Belter correlation
$\overline{Nu}$ = global averaged Nusselt number
Pr = Prandtl number
Re = Reynolds number based on the channel hydraulic diameter
ρ = density of the plexiglass, kg/m^3

Subscripts

i = initial condition
r = airflow condition
w = local wall surface value

References

[1] Kim, Y. W., Arellano, L., Vardakas, M., Moon, H. K., and Smith, K. O., 2003, "Comparison of Trip-Strip/Impingement/Dimple Cooling Concepts at High Reynolds Numbers," ASME Turbo Expo 2003, Power for Land, Sea, and Air, Atlanta, GA, ASME Paper No. GT2003-38935.
[2] Afanasyev, V. N., Chudnovsky, Y. P., Leontiev, A. I., and Roganov, P. S., 1993, "Turbulent Flow Friction and Heat Transfer Characteristics for Spherical Cavities on a Flat Plate," Exp. Therm. Fluid Sci., **7**(1), pp. 1–8.
[3] Terekhov, V. I., Kalinina, S. V., and Mshvidobadze, Y. M., 1997, "Heat Transfer Coefficient and Aerodynamic Resistance on a Surface With a Single Dimple," Enhanced Heat Transfer, **4**(2), pp. 131–145.
[4] Burgess, N. K., and Ligrani, P. M., 2005, "Effects of Dimple Depth on Channel Nusselt Numbers and Friction Factors," ASME J. Heat Transfer, **127**(8), pp. 839–847.
[5] Saini, R. P., and Verma, J., 2008, "Heat Transfer and Friction Factor Correlations for a Duct Having Dimple-Shape Artificial Roughness for Solar Air Heaters," Energy, **33**(8), pp. 1277–1287.
[6] Mitsudharmadi, H., Tay, C. M. J., and Tsai, H. M., 2009, "Effect of Rounded Edged Dimple Arrays on the Boundary Layer Development," J. Vis., **12**(1), pp. 17–25.
[7] Won, S. Y., and Ligrani, P. M., 2004, "Numerical Predictions of Flow Structure and Local Nusselt Number Ratios Along and Above Dimpled Surfaces With Different Dimple Depths in a Channel," Numer. Heat Tranf. A-Appl., **46**(6), pp. 549–570.
[8] Lan, J., Xie, Y., and Zhang, D., 2011, "Heat Transfer Enhancement in a Rectangular Channel with the Combination of Ribs, Dimples and Protrusions," ASME 2011 Turbo Expo: Turbine Technical Conference and Exposition, Vancouver, British Columbia, Canada, pp. 1447–1455, ASME Paper No. GT2011–46031.
[9] Xie, G., Liu, J., Ligrani, P. M., and Zhang, W., 2013, "Numerical Predictions of Heat Transfer and Flow Structure in a Square Cross-Section Channel With Various Non-spherical Indentation Dimples," Numer. Heat Tranf. A-Appl., **64**(3), pp. 187–215.
[10] Luo, L., Wen, F., Wang, L., Sunden, B., and Wang, S., 2017, "On the Solar Receiver Thermal Enhancement by Using the Dimple Combined With Delta Winglet Vortex Generator," Appl. Therm. Eng., **111**(1), pp. 586–598.
[11] Ligrani, P. M., Harrison, J. L., Mahmmod, G. I., and Hill, M. L., 2001, "Flow Structure due to Dimple Depressions on a Channel Surface," Phys. Fluids, **13**(11), pp. 3442–3451.
[12] Mahmood, G. I., Hill, M. L., Nelson, D. L., Ligrani, P. M., Moon, H. K., and Glezer, B., 2001, "Local Heat Transfer and Flow Structure on and Above a Dimpled Surface in a Channel," ASME J. Turbomach., **123**(1), pp. 115–123.
[13] Zhou, W., Rao, Y., and Hu, H., 2015, "An Experimental Investigation on the Characteristics of Turbulent Boundary Layer Flows Over a Dimpled Surface," ASME J. Fluid Eng., **138**(2), p. 021204.

[14] Moon, H. K., O'Connell, T., and Glezer, B., 2000, "Channel Height Effect on Heat Transfer and Friction in a Dimpled Passage," ASME J. Eng. Gas. Turbines Power, **122**(2), pp. 307–313.
[15] Mahmood, G. I., and Ligrani, P. M., 2002, "Heat Transfer in a Dimpled Channel: Combined Influences of Aspect Ratio, Temperature Ratio, Reynolds Number, and Flow Structure," Int. J. Heat Mass Transfer, **45**(10), pp. 2011–2020.
[16] Coy, E. B., and Danczyz, S. A., 2011, "Measurements of the Effectiveness of Concave Spherical Dimples for Enhancement Heat Transfer," J. Propul. Power, **27**(5), pp. 955–958.
[17] Chyu, M. K., Yu, Y., and Ding, H., 1999, "Heat Transfer Enhancement in Rectangular Channels With Concavities," Enhanced Heat Transfer, **6**(6), pp. 429–439.
[18] Neil Jordan, C., and Wright, L. M., 2012, "Heat Transfer Enhancement in a Rectangular (AR = 3:1) Channel With V-Shaped Dimples," ASME J. Turbomach., **135**(1), p. 011028.
[19] Rao, Y., Xu, Y., and Wan, C., 2012, "A Numerical Study of the Flow and Heat Transfer in the Pin Fin-Dimple Channels With Various Dimple Depths," ASME J. Heat Transfer, **134**(7), p. 071902.
[20] Han, J. C., and Park, J. S., 1988, "Developing Heat Transfer in Rectangular Channels With Rib Turbulators," Int. J. Heat Mass Transfer, **31**(1), pp. 183–195.
[21] Han, J. C., and Zhang, Y. M., 1992, "High Performance Heat Transfer Ducts With Parallel Broken and V-Shaped Broken Ribs," Int. J. Heat Mass Transfer, **35**(2), pp. 513–523.
[22] Fu, W. L., Wright, L. M., and Han, J. C., 2005, "Heat Transfer in Two-Pass Rotating Rectangular Channels (AR = 1:2 and AR = 1:4) With 45 Deg Angled Rib Turbulators," ASME J. Turbomach., **127**(1), pp. 164–174.
[23] Han, J. C., and Chen, H. C., 2006, "Turbine Blade Internal Cooling Passages With Rib Turbulators," J. Propul. Power, **22**(2), pp. 226–248.
[24] Choi, E. Y., Choi, Y. D., and Kwak, J. S., 2013, "Effect of Dimple Configuration on Heat Transfer Coefficient in a Rib-Dimpled Channel," J. Thermophys. Heat Transfer, **27**(4), pp. 653–659.
[25] Choi, E. Y., Choi, Y. D., Lee, W. S., Chung, J. T., and Kwak, J. S., 2013, "Heat Transfer Augmentation Using a Rib–Dimple Compound Cooling Technique," Appl. Therm. Eng., **51**(1–2), pp. 435–441.
[26] Singh, P., and Ekkad, S., 2017, "Experimental Study of Heat Transfer Augmentation in a Two-Pass Channel Featuring V-Shaped Ribs and Cylindrical Dimples," Appl. Therm. Eng., **116**(5), pp. 205–216.
[27] Singh, P., Pandit, J., and Ekkad, S. V., 2017, "Characterization of Heat Transfer Enhancement and Frictional Losses in a Two-Pass Square Duct Featuring Unique Combinations of Rib Turbulators and Cylindrical Dimples," Int. J. Heat Mass Transfer, **106**(3), pp. 629–647.
[28] Rao, Y., Feng, Y., Li, B., and Weigand, B., 2015, "Experimental and Numerical Study of Heat Transfer and Flow Friction in Channels With Dimples of Different Shapes," ASME J. Heat Transfer, **137**(3), p. 031901.
[29] Chyu, M. K., Yu, Y., Ding, H., Downs, J. P., and Soechting, F. O., 1997, "Concavity Enhanced Heat Transfer in an Internal Cooling Passage," ASME 1997 International Gas Turbine and Aeroengine Congress and Exhibition, Orlando, FL, V003T09A080.
[30] Chang, S. W., Chiang, K. F., and Chou, T. C., 2010, "Heat Transfer and Pressure Drop in Hexagonal Ducts With Surface Dimples," Exp. Therm. Fluid Sci., **34**(8), pp. 1172–1181.
[31] Soloff, S. M., Adrian, R. J., and Liu, Z. C., 1997, "Distortion Compensation for Generalized Stereoscopic Particle Image Velocimetry," Meas. Sci. Technol., **8**(12), pp. 1441–1454.
[32] Ligrani, P. M., Oliveira, M. M., and Blaskovich, T., 2003, "Comparison of Heat Transfer Augmentation Techniques," AIAA J., **41**(3), pp. 337–360.
[33] Han, J. C., 2006, "Turbine Blade Cooling Studies at Texas A&M University: 1980–2004," J. Thermophys. Heat Transfer, **20**(2), pp. 161–187.
[34] Kays, V. M., and Crawford, M.E., 1993, *Convective Heat and Mass Transfer*, McGraw-Hill Education, New York.
[35] Gee, D. L., and Webb, R. L., 1980, "Forced Convection Heat Transfer in Helically Rib-Roughened Tubes," Int. J. Heat Mass Transfer, **23**(8), pp. 1127–1136.
[36] Ligrani, P. M., Burgess, N. K., and Won, S. Y., 2005, "Nusselt Numbers and Flow Structure on and Above a Shallow Dimpled Surface Within a Channel Including Effects of Inlet Turbulence Intensity Level," ASME J. Turbomach., **127**(2), pp. 321–330.